Radially organized pillars in TiO2 and in TiO2/C microspheres: synthesis, characterization and photocatalytic tests

Radially organized pillars in TiO_2 and in TiO_2/C microspheres: synthesis, characterization and photocatalytic tests.

Federico Cesano[a*], Diego Pellerej[a], Domenica Scarano[a], Gabriele Ricchiardi[a] and Adriano Zecchina[a]

[a]*Nanostructured Interfaces and Surfaces (NIS), Centre of Excellence, Department of IFM Chemistry, University of Torino, Via Giuria 7, I-10125 Torino (Italy).*

[*]CORRESPONDING AUTHOR: Federico Cesano, Ph: +39 011 6707834, fax: +39 011 6707855, Via Giuria 7, I-10125 Torino (Italy), e-*mail:*federico.cesano@unito.it.

KEYWORDS: Mesoporous TiO_2 microspheres, TiO_2 pillars, Anatase/rutile, tunable composition, high photoactivity.

ABSTRACT: Porous TiO_2 microspheres with robust texture and high photoactivity, were prepared by inflowing a TiO_2 precursor in the confined space of *polystyrene-co-divinyl benzene* (PS-co-DVB) polymer, working as sacrificial scaffold. The impregnated polymer spheres, upon thermal treatments under N_2, N_2/air or pure air flow at temperatures in the 400-500°C interval, are transformed into porous microspheres. Depending on the gas flow composition, the obtained microspheres are constituted by porous carbon, hybrid core-shell C/TiO_2 or of cemented TiO_2 nanoparticles assembled in elongated pillars. The composition of pure TiO_2 microspheres ranges from pure anatase (400°C) to the prevailing rutile phase (>475-500°C). All samples have been extensively characterized by means of SEM/AFM microscopies, N_2-volumetric porosimetry, XRD and UV-Vis analyses. The photodegradation of NO has been used to check the photocatalytic activity of the TiO_2 materials. It is concluded that they exhibit higher photoactivity than the classical benchmark material (Degussa P25). This property together porous character of the microspheres, the tunable anatase-rutile ratio and the high cristallinity make these microspheres very interesting materials for applications in photocatalysis. From a physical point of view, the large axial pores and the columnar nature of the spheres can produce the entrapment of the light into the material.

1. INTRODUCTION

TiO_2 based materials with tailored shape, porosity, crystal sizes and composition, are attracting great attention because of their use in application fields, such as photocatalysis and energy conversion [1-6]. As far as photocatalysis is concerned, many factors are known to play a key role, such as crystallinity, phase composition and surface area [1-3, 7-11]. In particular it has been reported that mixed anatase/rutile TiO_2 materials may exhibit higher photocatalytic efficiency because their light harvesting efficiency may be favored by the presence of the rutile phase, characterized by a lower energy-gap and a more pronounced absorption in the visible and because of anatase/rutile junctions, might promote the charge separation in the surface region and the reduction of the combination of photogenerated electrons and holes [11-15]. This can be the explanation of the high activity of Degussa P25, a mixture of 85-80%wt anatase and 15-20%wt rutile nanoparticles, widely recognized as a benchmark material. As photocatalysis is involving the formation and the adsorption/desorption of reactants and products,

surface area, nanocrystals morphology, the structure, and the exposed habit (in particular the dominant presence of anatase-exposed {001} facets) [3, 10, 16-19], are also playing a primary role [7, 12]. Beside the presence of rutile, peculiar defects of TiO_2 materials acting as trap sites for photoexcited charge carriers [20], particle structuring at different length scales and spatial organization of the TiO_2 nanoparticles [21], doping with light and heavy elements (B, C, N, S, F, Br, Cl) or metals, can increase the visible light absorption and the photon efficiency [3, 22-28].

The presence of single nanoparticles characterized by high photocatalytic activity is not, however, the sole requisite for practical applications. In fact in industrial applications, the separation of TiO_2 material from the solution after irradiation is necessary and constitutes an important requirement for an efficient use of the material [29] as well as the presence of a hierarchical porosity provides, on one hand a fast accessibility and a facile fluid transport of matter (larger pores) and on the other hand, the increased surface contact (smaller pores) [15]. As this efficient separation is not obtainable when the material is highly dispersed, TiO_2 samples containing robust microaggregates of cemented nanoparticles, characterized by intrinsic mesoporosity and high surface area, may facilitate the separation of the photocatalyst from the reaction medium [7]. Although the formation of nanoparticles agglomerates is accompanied by some surface area decrements, the resulting activity is not necessarily decreased because the interparticle charge transfer can advantageously act as compensating factor [7].

Several approaches to control size, shape and agglomeration state of TiO_2 nanoparticles have been attempted [4]. Nanotubes [30], nanorods [31, 32], monolithic porous structures [15, 33, 34], inverse opals [35] and microspheres [19, 36-41] have been studied.

Among all investigated approaches, the template-based procedures look ideal to control the TiO_2 structure because the pore size distribution of the templating scaffold, where the desired material is formed, can be properly tailored [21, 29, 42]. In this paper, we describe a new method for the synthesis of spherical TiO_2-based porous aggregates, starting from porous polymer microspheres impregnated with a Ti molecular precursor. Depending on the synthesis conditions, from inert to oxidizing atmosphere, the resulting products are ranging from an amorphous composite systems, to pure TiO_2 microspheres with selected anatase/rutile compositions.

The TiO_2 microspheres appear to be very robust because constituted by highly crystalline cemented nanoparticles and they have surface area comparable with that of P25. The catalyst texture and structure was determined by XRD, SEM, AFM, N_2-adsorption isotherms and UV-Vis spectroscopy. NO photodegradation tests on TiO_2 microspheres demonstrate that they are highly active and that the activity is influenced by the crystallinity, morphology, and by the anatase-rutile ratio.

This work provides new insights on the morphology, structure, phase composition and cristallinity with regard to the photocatalytic activity of TiO_2. This matter is of a broad and significative interest in photocatalysis and in the energy conversion fields.

2. MATERIAL AND METHODS

2.1 Sample preparation. Poly[styrene-co-(divinyl benzene)] (PS-co-DVB) polymer microspheres as scaffold and Ti isopropoxyde (TIP) from Aldrich as titania precursor, were used.

The preparation of materials is shown in Scheme 1. The polymer microspheres were first impregnated under stirring for 24h in a solution 1:1 v/v of TIP in isopropyl alcohol. The solution was then filtered and dried (Scheme 1, Step a).

The dried polymer was then treated under gas flow following different paths : 1) N_2 gas flow at 500°C for 2 h (scaffold pyrolysis) (Scheme 1: Step b, path 1); 2) N_2-air flow for 15' at 500°C (Scheme 1: step b, path 2) (partial combustion of the polymer scaffold); 3) N_2-air flow for 2h at temperatures comprised

in the 400°C-500°C range (complete combustion of the scaffold) (Scheme1: Step b, paths 3). Time and temperature parameters of oxidation path 3 were selected step by step in order to obtain materials with specific phase compositions, ranging from anatase to rutile phase.

2.2 Characterization techniques. The morphology of the sample has been investigated by means of SEM (Zeiss Evo50) equipped with an Oxford energy dispersive X-ray detector), by FESEM (ZEISS SUPRA 40) equipped with a field emission tungsten cathode, AFM (Park Systems XE-100). The crystallinity and the phase composition of samples have been estimated by XRD analysis (PANalytical X'Pert PRO diffractometer equipped with a Ni filtered Cu radiation in a standard Bragg−Brentano geometry). Diffuse reflectance UV-vis spectra have been recorded directly on the materials at room temperature by means of a UV-Vis spectrometer (Varian Cary UV 5000) equipped with a diffuse reflectance attachment. Materials used for the UV-Vis analysis (nanoanatase, anatase and rutile from Aldrich) were diluted in $BaSO_4$ to obtain a correct intensity.

N_2 adsorption–desorption experiments have been carried out at 77K (Micromeritics ASAP 2020 instrument) to determine the Brunauer–Emmett–Teller (BET) surface area and micropore volume (t-plot method). Before the surface area determination, the samples were degassed at 150°C for 5-6h. The pore size distributions (PSDs) were obtained by means of a non-negative least squares fitting on the absorption isotherm data by applying Density Functional Theory (DFT) models (N2-DFT model, slit geometry) of ASAP 2020 4.0 software (Micromeritics). Microporous (S_{MICRO}) and mesoporous (S_{MESO}) surfaces were obtained from t-plot and from $S_{MESO} = S_{TOT} - S_{MICRO}$, respectively.

2.3 Photocatalytic tests. In a typical photocatalytic test, the sample (~0.05 g) is placed in a glass flow reactor exposed to a continuous gas flow of He (60 ml/min) containing 4.5 ppm of NO. The reaction is kept in the dark for 1h, in order to reach the adsorption equilibrium.

Then, the reactor is irradiated in a solar box for 1h. The test continues for at least four alternating light cycles on/off (see Supplementary Material).

Please, insert here Scheme 1.

3. RESULTS AND DISCUSSION

The commercial microporous *PS-co-DVB* polymer (surface area ≈1000 m^2/g) is SEM and AFM imaged in Figure 1a-c. The sample is constituted by apparently rounded polymer microspheres with diameters comprised in the 400÷600 μm range (Figure 1a and inset therein).

Please, insert here Figure 1.

Rare cracks and surface defects are identified at higher magnification by image contrast (arrows in Figure 1a). The microspheres are constituted by nanodomains 20÷80 nm in size, as obtained by AFM height profile (inset of Figure 1b). The pore size distribution, as obtained by DFT (density functional theory) model applied on the N_2 adsorption isotherm at 77K, shows that the pores diameter is ranging in the 8÷20 nm interval (Figure 1c).These domains are large enough to allow the easy accessibility to incoming molecules.

3.1 TiO_2/C COMPOSITE MICROSPHERES FROM PATH 1) AND 2): MORPHOLOGY AND STRUCTURE

SEM images of the sample obtained from TIP impregnated polymer microspheres and then pyrolyzed under N_2 gas flow at 500°C (path 1) are shown in Figure 2a-c. The pyrolyzed sample is in form of microspheres with contracted diameter in the 150÷200 μm range (Figure 2a and Supplementary Material).

Please, insert here Figure 2.

At low magnification, the pyrolyzed microspheres with spherical shape expose an apparently regular surface (Figure 2a). At higher magnification prominent scratches, irregularly distributed and several microns spaced, are observable (Figure 2b). They are plausibly associated with those observed on the raw polymer spheres (see Figure 2a). The high resolution SEM/AFM images evidence that the apparently flat portions of the surface are actually irregular and composed by aggregates of 50÷300 nm size. The composition is dominated by C and Ti signals (inset of Figure 2c).

The size contraction of microspheres induced by the thermal pyrolysis is associated with a decrease of the surface area from ~1000 m^2/g (data not reported) to ~ 200 m^2/g (*vide infra*).

It will be shown that the sample is essentially characterized by micropores with diameter in the 10÷20 nm range and that mesopores in a wide range distribution are also present.

When the sample is treated under mild oxidative conditions following Step 2b of Scheme 1, (500°C, air flow for 15') (path 2), the diameters of spheres are retained in the 200÷400 μm interval (Figure 3a). The surface of the microspheres is completely modified and here dominated by the presence of islands (Figure 3b) constituted by cemented nanoparticles (Figure 3c). These islands are the termination of elongated structures plausibly implanted on a more dense core (Figure 3d). About the arrangement of the elongated structures we shall return in the following, when the fully oxidized samples will be discussed. The chemical composition of the outer layer is dominated by Ti and O, whereas the internal phase is constituted by Ti and C.

Please, insert here Figure 3.

XRD patterns of samples thermally treated at 500°C under N_2 and N_2/air gas mixture are shown in Figure 4. In this figure, it clearly evidenced that upon thermal treatment under pure N_2, a carbonaceous amorphous phase is obtained with no information about the state of Ti. Upon mild air oxidation, a composite composition, constituted by crystalline anatase and rutile nanoparticles (≈65:35 w/w) with the minor presence of the carbonaceous phase, is obtained. The application of Scherrer's equation [43] on the (101) and (110) XRD diffractions peaks of anatase and rutile, located at about 2θ≈25.3° and 2θ≈27.4°, respectively, allows to obtain the values of the mean crystal size of each phase (~16 and ~34 nm, respectively). This result is in broad agreement with the SEM/AFM results.

Please, insert here Figure 4.

The porous structure of the outer layer is due to TiO_2 nanoparticles assembled in pillars, which are protruding from an internal core constituted by amorphous carbon.

In conclusion, during mild oxidative treatments carbon is fully removed by oxidation only in the external part of the microspheres, leading to the formation of core/shell C/TiO_2 microspheres with robust nature, because constituted by TiO_2 cemented anatase/rutile nanoparticles assembled in elongated pillars, which are embedded in a carbon matrix.

3.2 TIO_2 PURE MICROSPHERES FROM PATH 3): MORPHOLOGY AND STRUCTURE

In order to gain a complete combustion of the carbonaceous component and simultaneously control the anatase/rutile ratio, a series of oxidation experiments have been performed, by modifying the oxidation temperature from 400°C to 500°C (Step 2c, Scheme 1) for longer time (2h).

A single sphere of 300 μm, as obtained from oxidation at 500°C, is SEM and AFM imaged in Figure 5a-d. The spheres are porous and the shape is retained even after full elimination of carbon (Figure 5a). The same is observed also for lower temperature treatments (400°C, 450°C and 475°C) and the microspheres all have sizes in the 150-350 μm range. At higher magnification, the sphere reveals a porous structure constituted by elongated pillars protruding from the core (Figure 5b). The pillar heads have irregular contours with 5-10 μm size and appears constituted by nanoparticles of 25-50nm (Figure 5c-d). The sharp edges of a pillar head is AFM imaged in Figure 5d.

Please, insert here Figure 5.

XRD patterns, phase composition and crystal sizes of microspheres obtained at 400°C, 450°C, 475°C and at 500°C are reported in Figure 6 and in Table 1.

Please, insert here Figure 6 and Table 1.

From these results, it is clearly emerging that the oxidation temperature plays a crucial role in determining the anatase/rutile ratio, the crystallinity and particle sizes. Furthermore, it can be concluded that the composition of microspheres can be finely tuned, from the pure anatase phase (400°C) to the prevailing rutile composition.

3.3 Surface and optical properties of carbon/TiO_2 composite and of pure TiO_2 microspheres

Volumetric N_2 adsorption/desorption isotherms and pore size distributions of the obtained microspheres are shown in Figure 7. BET surface area (S_{BET}), Microporous (S_{micro}) and mesoporous (S_{meso}) surface area properties of samples are reported in Table 2.

Please, insert here Figure 7 and Table 2.

In addition to the macroporosity observed by SEM, from the isotherm shape of the samples not fully oxidized (Figure 7a), a mixed micropores/mesoporous character is inferred. The isotherms of the samples entirely oxidized (at 400°C, 450°C, 475°C and et 500°C) are reported in Figure 7b. All these isotherms are of type IV with large hysteresis loops, thus indicating the mesoporous nature of samples and the negligible contribution of small micropores.

All these results are confirmed by pore size distribution (PSDs) reported in Figure 7c. More in detail, the pyrolized microspheres (black circles) and the core/shell C/TiO_2 microspheres (grey circles), obtained from path 1 and 2) respectively, are essentially microporous (two families of micropores in the 8-20Å range) with a wide and complex mesopore distribution. The micropores are absent on fully oxidized samples obtained from path 3), while the mesopore contribution decreases in intensity with the increase of the treatment temperature: 400°C (magenta circles), 450°C (blue circles), 475°C (green circles) and 500°C (red circles). These PSD obtained from DFT model are fully supported by the same calculated by BJH (Barrett-Joyner-Halenda) method from the desorption branches of the N_2-isotherms (see Supplementary Material). The temperature of treatment has also a drastic effect on the surface area (S_{BET}), which is decreasing from 163 m^2/g (400°C) to 44 m^2/g (500 °C).

The optical properties of the carbon-free microspheres synthesized in the 400-500 °C interval have been monitored by UV-Vis spectroscopy in the reflectance mode and the results obtained in the 23000-

28000 cm^{-1} interval are shown in Figure 8. In the same figure the spectra of reference materials (nanoanatase, anatase and rutile), are reported for comparison.

Please, insert here Figure 8.

From this figure, it can be inferred that the absorption edge moves from a position similar to that of commercial nanoanatase (but lower than that of anatase constituted by large crystallites due to the quantum confinement effect) to that of rutile. The sample synthesized at 450°C (containing ≈25%wt rutile) shows an adsorption edge profile similar to that of P25.

In conclusion, the accurate control of the temperature and of the gas phase composition allows to tailor the mesoscopic and microscopic structure of the microspheres.

As far as the mechanism formation of porosity is concerned, on the basis of the obtained results and of the current literature, we can state that the microporous polimer scaffold retains the spherical shape of the microspheres upon the thermal treatment avoiding the collapsing of material, but obviously, cannot explain alone the formation of a hyrarchical porosity. Some authors proposed some models for the formation of a simoultaneous macro/mesoporosity. According to these mechanisms [44-47], we can assume that the contact between the Ti precursor and alcohol/water media produces a thin and semipermeable TiO_2 membrane constituted by dimers, trimers, tetramers, …, which are then subjected to subsequent hydrolisys and condensation reactions. At moderate temperature the self-aggregation of these TiO_2 particles takes place via their condensation, giving rise to the interparticle porosity (smaller pores) [34], while the nanoblocks will arrange into high-ordered superstructures (larger pores) [18]. It is notewhorthy that the porous structure of the TiO_2 microspheres is almost preserved upon the thermal treatments. This fact makes these materials interesting for application in photocatalysis.

3.4 NO PHOTO-OXIDATION TESTS

The photocatalytic oxidation of NO to NO_2 has been chosen as test of the photocatalytic activity for two reasons:

- the testing method of NO photodegradation is well known and standardized [48, 49].
- NO, O_2, NO_2 can easily diffuse in and out through the interparticle interstices into the mesopores of the samples (and hence the obtained data are not affected by diffusion problems).

The results of a typical photocatalytic degradation experiment are shown in Figure 9a, where the [NO] decreases from the concentration obtained in the dark (top plateau) upon light irradiation (bottom plateau). In the same figure the formation of NO_2 during the same cycles is also illustrated.

Please, insert here Figure 9.

It can be clearly seen that during the irradiation period, a quick decrease of the NO concentration takes place, which is accompanied by the formation of NO_2. After the first two-three light/dark cycles the NO concentrations become stable and the NO convesion (%) can be obtained. Details about the set-up and experimental conditions are reported in the Supplementary Material pharagraph. These results are in full agreement with those reported in refs. [48, 49]. The catalytic efficiency of each sample was calculated after the completion of 3 cycles, which is the number of cycles necessary to achieve a stable response of the catalyst.

The phodegradation experiments have been performed on the samples oxidized at 400, 450, 475 and 500°C described before. In Figure 9b the activities (average of two experiments) normalized by weight

(i.e. obtained on the same amount of powder), are compared. In Figure 9c the activities normalized by surface area as well, are compared. In the same figures the activity of P25 is also reported for comparison. The samples utilized in these tests were the same characterized by XRD and BET.

The error bars of Figure 9b and c are characteristic of the set-up detection system. The results of photocatalytic tests conducted on samples belonging to different series, have demonstrated that error bars of Figure 9b are representative. The larger error bars of Figure 9c, being surface normalized, are affected by the uncertainty of the BET surface area measurement.

From Figure 9b it can be inferred that the catalysts efficiency of the samples of the whole 400, 450, 475 and 500°C series, compares very well with that of P25. Only the sample synthesized at 400°C (containing ≈100% anatase and with the highest surface area) looks slightly more active.

Our preparation method leads to tailored mesoporous anatase/rutile systems characterized by comparable surface area, tuneable phase composition and crystallinity. They can be used as benchmark for the investigation of photocatalytic properties.

In particular, the following hypothesis can be tested:

a) as the fraction of rutile increases along the 400-500°C series, the edge shifts to lower frequencies and the amount of harvested solar light is expected to increase as well. In principle this can potentially favour photocatalytic efficiency along the series;

b) as photocatalysis is a surface mediated process, the decrement of surface area observed along the 400-500°C series is expected to potentially work against efficiency;

c) as the fraction of rutile phase (that is considered less photoactive) [20] increases along the 400-500°C series, the efficiency is expected to decrease;

d) as the bulk defects population decreases along the 400-500°C series the efficiency is expected to increase in a parallel way along the series,

e) if the anatase/rutile junctions are vital for photacatalytic efficiency, the sample synthesized at 400°C (pure anatase) should show an unfavourable photocatalytic behaviour.

Which of these factors, often working in opposite directions, are determining the final activity will be discussed in the following on the basis of experimental results.

The results of Figure 9b show clearly that the photocatalytic efficiency of the microspheres is at least as high as that of P25. This fact together with the micrometric dimension and robustness make the microspheres ideal for photocatalytic applications in solution.

As for the role of the rutile/anatase ratio, of surface area and of defects concentration in determining the activity along the 400, 450, 475 and 500°C series, it can be inferred that, being the rutile phase completely absent in the 400°C sample, the presence of anatase/rutile junctions does not play a major role in determining the photoactivity of our systems.

The results of the 400°C sample seem also to suggest that surface area is a dominant factor. However when the surface area-normalized activities are compared (Figure 9c), it can be seen that also this hypothesis is not valid. In fact the surface normalized activity of the 400°C sample is the lowest! Another paradoxical result of Figure 9c is that samples with lowest surface area and highest rutile concentration show the highest activity. As the superior activity of anatase is fully ascertained in the literature [10, 24, 50], the sole conclusion which can be derived from the Figure 9c is that defects concentration, decreasing with the increase of oxidation temperatures, is the primary factor determining the activity of our systems. This conclusion is not excluding that the other minor factors are also playing a role. This conclusion can contribute to explain why P25 is such a good benchmark photocatalyst. In

fact, being P25 synthesized during a high temperature process (flame photolysis), thermal annealing is highly favoured and hence the bulk defect concentration influencing the electron-hole recombination, is minimized.

A further phenomenon favouring the activity of samples with large columnar pores (despite their lower surface area) could be the deeper penetration of light in the microspheres. In fact the structure of pores might act as a waveguide [21].

4. CONCLUSIONS

Mesoporous TiO_2 microspheres can be prepared by inflowing a TiO_2 precursor (Ti isopropoxyde) in the confined space of *polystyrene-co-divinyl benzene* (*PS-co-DVB*) polymer microspheres, working as sacrificial scaffold. Depending on the gas flow composition and temperature, the samples, prepared by combustion of the polymeric scaffold, are in form of microspheres constituted by hybrid core-shell C/TiO_2 or of cemented TiO_2 nanoparticles. The microspheres are mechanically very robust, mesoporous and characterized by high surface area. By tuning the gas composition and the combustion temperature, the phase composition of TiO_2 microspheres can be tailored from pure anatase (oxidation at 400°C) to a prevailing rutile phase (oxidation at 500°C). All samples have been extensively characterized by means of SEM/AFM microscopies, N_2-volumetric porosimetry, XRD and UV-Vis analyses. The fine tuning of the phase composition, surface area and crystallinity, allowed by the preparation procedure, has stimulated the study of the influence of these factors on photacatalytic activity. To this end the photodegradation of NO has been used as a test reaction. It is concluded that: i) all samples exhibit a photoactivity (normalized by weight of catalyst) as high or even higher than that of the classical benchmark material (Degussa P25); ii) the bulk defects concentration is the primary factor influencing the catalytic efficiency. Furthermore, the robust character of the microspheres, together with their permeability due to their mesoporous nature, the columnar nature of the TiO_2 phase favouring the entrapment of the light into the material along a preferential direction, makes them a very interesting materials not only for gas phase photocatalysis but also for photocatalytic applications in solution, where the catalyst recovery and separation are essential.

SUPPLEMENTARY DATA. Additional SEM images, particle size distributions, BJH pore size distributions, and photocatalytic test parameters are available.

ACKNOWLEDGMENTS

The authors thank MIUR and INSTM Consorzio for the financial supports.

REFERENCES

[1] Chen X, Mao SS. Chemical Reviews 107 (2007); 2891-959.
[2] Chen X, Shen S, Guo L, Mao SS. Chemical Reviews 110 (2010); 6503-70.
[3] Diebold U. Surface Science Reports 48 (2003); 53-229.
[4] Nair AS, Peining Z, Babu VJ, Shengyuan Y, Ramakrishna S. Physical Chemistry Chemical Physics 13 (2011); 21248-61.
[5] Xiang Q, Yu J, Jaroniec M. Chemical Society Reviews 41 (2012); 782-96.
[6] Uddin MJ, Cesano F, Bonino F, Bordiga S, Spoto G, Scarano D, et al. J Photochem Photobiol A-Chem 189 (2007); 286-94.

[7] Lakshminarasimhan N, Bae E, Choi W. J Phys Chem C 111 (2007); 15244-50.
[8] Tanaka K, Capule MFV, Hisanaga T. Chemical Physics Letters 187 (1991); 73-6.
[9] Ohno T, Sarukawa K, Matsumura M. The Journal of Physical Chemistry B 105 (2001); 2417-20.
[10] Selloni A. Nature 7 (2008); 613-5.
[11] Zhang J, Xu Q, Feng Z, Li M, Li C. Angew Chem-Int Edit 47 (2008); 1766-9.
[12] Hurum DC, Gray KA, Rajh T, Thurnauer MC. J Phys Chem B 109 (2005); 977-80.
[13] Porter JF, Li YG, Chan CK. Journal of Materials Science 34 (1999); 1523-31.
[14] Kawahara T, Konishi Y, Tada H, Tohge N, Nishii J, Ito S. Angew Chem-Int Edit 41 (2002); 2811-+.
[15] Yu JG, Su YR, Cheng B. Advanced Functional Materials 17 (2007); 1984-90.
[16] Yang HG, Sun CH, Qiao SZ, Zou J, Liu G, Smith SC, et al. Nature 453 (2008); 638-41.
[17] Liu S, Yu J, Jaroniec M. J Am Chem Soc 132 (2010); 11914-6.
[18] Liu S, Yu J, Jaroniec M. Chem Mat 23 (2011); 4085–93.
[19] Yu J, Xiang Q, Ran J, Mann S. CrystEngComm 12 (2010); 872-9
[20] Cheng H, Selloni A. Journal of Chemical Physics 131 (2009).
[21] Aprile C, Corma A, Garcia H. Physical Chemistry Chemical Physics 10 (2008); 769-83.
[22] Grirrane A, Corma A, Garcia H. Science 322 (2008); 1661-4.
[23] Asahi R, Morikawa T, Ohwaki T, Aoki K, Taga Y. Science 293 (2001); 269-71.
[24] Sun Q, Xu Y. The Journal of Physical Chemistry C 114 (2010); 18911-8.
[25] Usseglio S, Damin A, Scarano D, Bordiga S, Zecchina A, Lamberti C. Journal of the American Chemical Society 129 (2007); 2822-8.
[26] Uddin MJ, Cesano F, Scarano D, Bonino F, Agostini G, Spoto G, et al. J Photochem Photobiol A-Chem 199 (2008); 64-72.
[27] Uddin MJ, Cesano F, Bertarione S, Bonino F, Bordiga S, Scarano D, et al. J Photochem Photobiol A-Chem 196 (2008); 165-73.
[28] Luo HM, Takata T, Lee YG, Zhao JF, Domen K, Yan YS. Chem Mat 16 (2004); 846-9.
[29] Shchukin DG, Schattka JH, Antonietti M, Caruso RA. J Phys Chem B 107 (2003); 952-7.
[30] Cesano F, Bertarione S, Uddin MJ, Agostini G, Scarano D, Zecchina A. J Phys Chem C 114 (2011); 169-78.
[31] Shi J, Sun C, Starr MB, Wang X. Nano Letters 11 (2011); 624-31.
[32] Limmer SJ, Cao G. Advanced Materials 15 (2003); 427-31.
[33] Cesano F, Bertarione S, Damin A, Agostini G, Usseglio S, Vitillo JG, et al. Advanced Materials 20 (2008); 3342.
[34] Yu J, Zhang L, Cheng B, Su Y. J Phys Chem C 111 (2007); 10582–9.
[35] Sordello F, Duca C, Maurino V, Minero C. Chemical Communications 47 (2011); 6147-9.
[36] Yu JG, Guo HT, Davis SA, Mann S. Advanced Functional Materials 16 (2006); 2035-41.
[37] Xia YD, Mokaya R. Journal of Materials Chemistry 15 (2005); 3126-31.
[38] Shchukin DG, Caruso RA. Chem Mat 16 (2004); 2287-92.
[39] Lei ZB, Li JM, Ke YX, Zhang YG, Zhang HC, Li FQ, et al. Journal of Materials Chemistry 11 (2001); 2930-3.
[40] Caruso RA, Susha A, Caruso F. Chem Mat 13 (2001); 400-9.
[41] Yang S-C, Yang D-J, Kim J, Hong J-M, Kim H-G, Kim I-D, et al. Advanced Materials 20 (2008); 1059.
[42] Kondo JN, Yamashita T, Nakajima K, Lu D, Hara M, Domen K. Journal of Materials Chemistry 15 (2005); 2035-40.

[43] Rahman MM, Cesano F, Bardelli F, Scarano D, Zecchina A. Catalysis Today 150 (2010); 84-90.
[44] Yu J, Su Y, Cheng B. Advanced Functional Materials 17 (2007); 1984.
[45] Collins A, Carriazo D, Davis SA, Mann S. Chemical Communications 5 (2004); 568–9.
[46] Yu J, Liu S, Yu H. Journal of Catalysis 249 (2007); 59-66.
[47] Yu J, Yu C, Leung MK-P, Ho W, Cheng B, Zhao X, et al. Journal of Catalysis 217 (2003); 69-78.
[48] Sadanaga Y, Matsumoto J, Kajii Y. J Photochem Photobiol C-Photochem Rev 4 (2003); 85-104.
[49] Devahasdin S, Fan C, Li KY, Chen DH. J Photochem Photobiol A-Chem 156 (2003); 161-70.
[50] Xu M, Gao Y, Moreno EM, Kunst M, Muhler M, Wang Y, et al. Phys Rev Lett J1 - PRL 106 (2011); 138302.

SCHEMES.

Scheme 1. Preparation steps of micropheres: a) impregnation/stirring and drying of the PS-co-DVB polymer spheres in an alcohol solution of TIP; b1) under pure N_2 at 500°C; b2) under air/N_2 mixtures at 500°C for 15'; b3) under air/N_2 mixtures at 400°C; 450°C and 475°C and at 500°C for 2h.

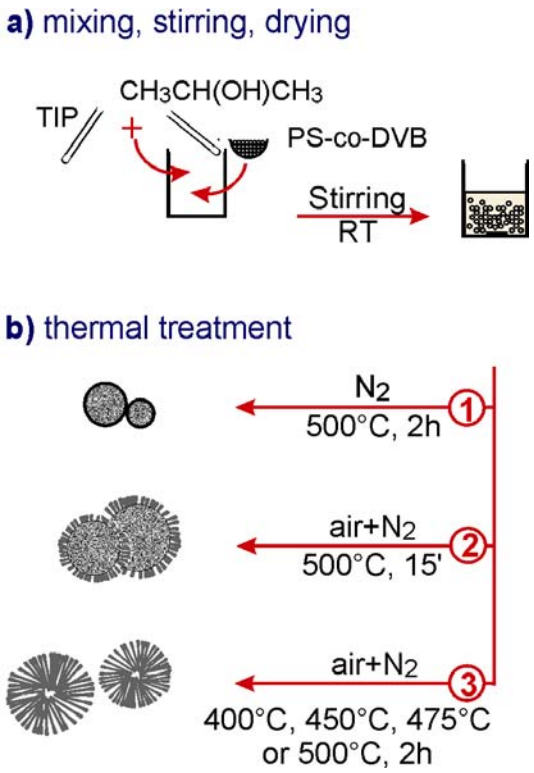

TABLES

Table 1. Semi-quantitative XRD data of the samples.

Temperature of treatment (°C)	Anatase		Rutile	
	(%)[i]	Cryst. size[ii] (nm)	(%)[i]	Cryst. size[ii] (nm)
400°C, N_2/air	99	8	-	-
450°C, N_2/air	74	11	26	15
475°C, N_2/air	39	21	61	26
500°C, N_2/air	24	22	76	30

[i]Phase compositions of the samples were obtained from reference intensity ratio (RIR) values of XRD standards (anatase and rutile); [ii]Obtained by applying the Sherrer equation on (101) and (110) XRD plane reflections of the Anatase and of the Rutile phases.

Table 2. Specific Surface area (SSA) of samples

Temperature of treatment (°C)	**S_{BET} (m^2/g)**	**S_{micro} (m^2/g)**	**S_{meso} (m^2/g)**
Carbonaceous microspheres:			
500°C, N_2	186	154	32
Core-shell C/TiO_2 composite microspheres:			
500°C, N_2/air 15’	76	36	40
Pillared TiO_2 microspheres:			
400°C, air 2h	163		163
450°C, air 2h	78	-	78
475°C, air 2h	58	-	58
500°C, air 2h	44	-	44

FIGURES AND FIGURE CAPTIONS.

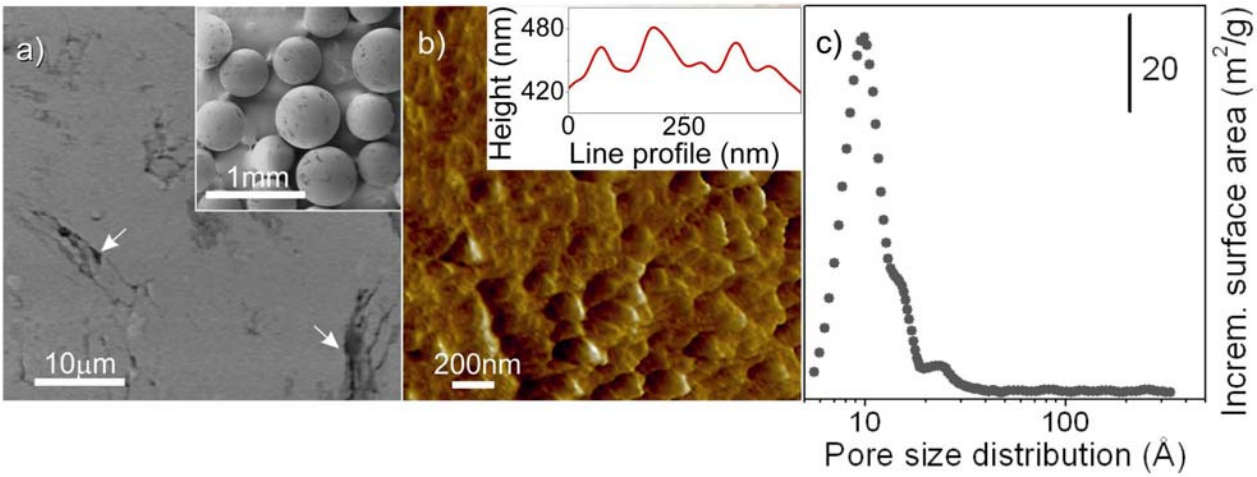

Figure 1. a) SEM image of a polymer microsphere. The arrows indicate cracks and fractures on the surface; b) 2x2 μm AFM topography of the surface and c) pore size distribution (PSD) of the polymer spheres. In the inset of a) and b) some polymer microsphere are SEM imaged and the height profile along a selected line of the AFM image is shown, respectively.

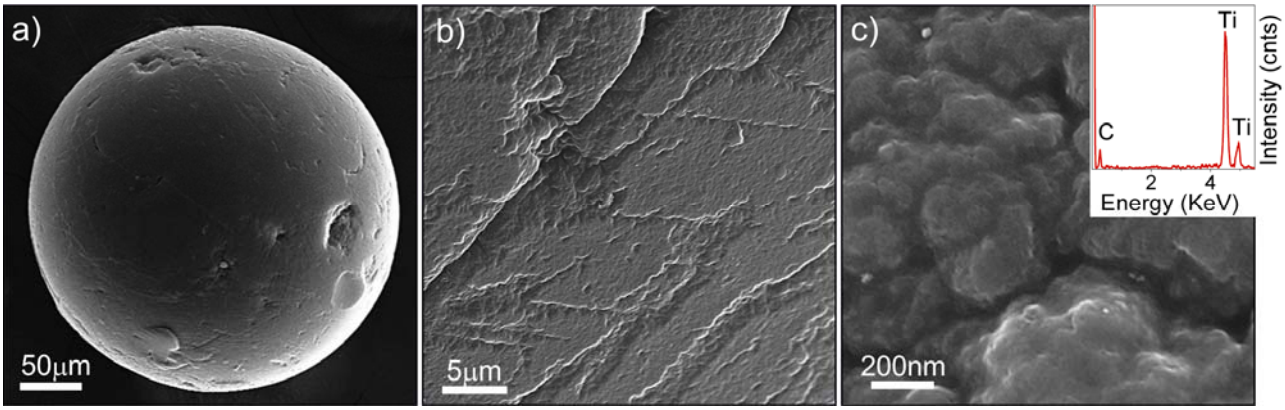

Figure 2. SEM images of TIP/PS-co-DVB polymer microspheres after carbonization under N_2 at 500°C, taken at increasing magnification: a) SEM image of a microsphere; b) and c) SEM enlarged views of selected regions on a sphere. In the inset of c) EDAX elemental analysis taken on a portion of a microsphere is shown.

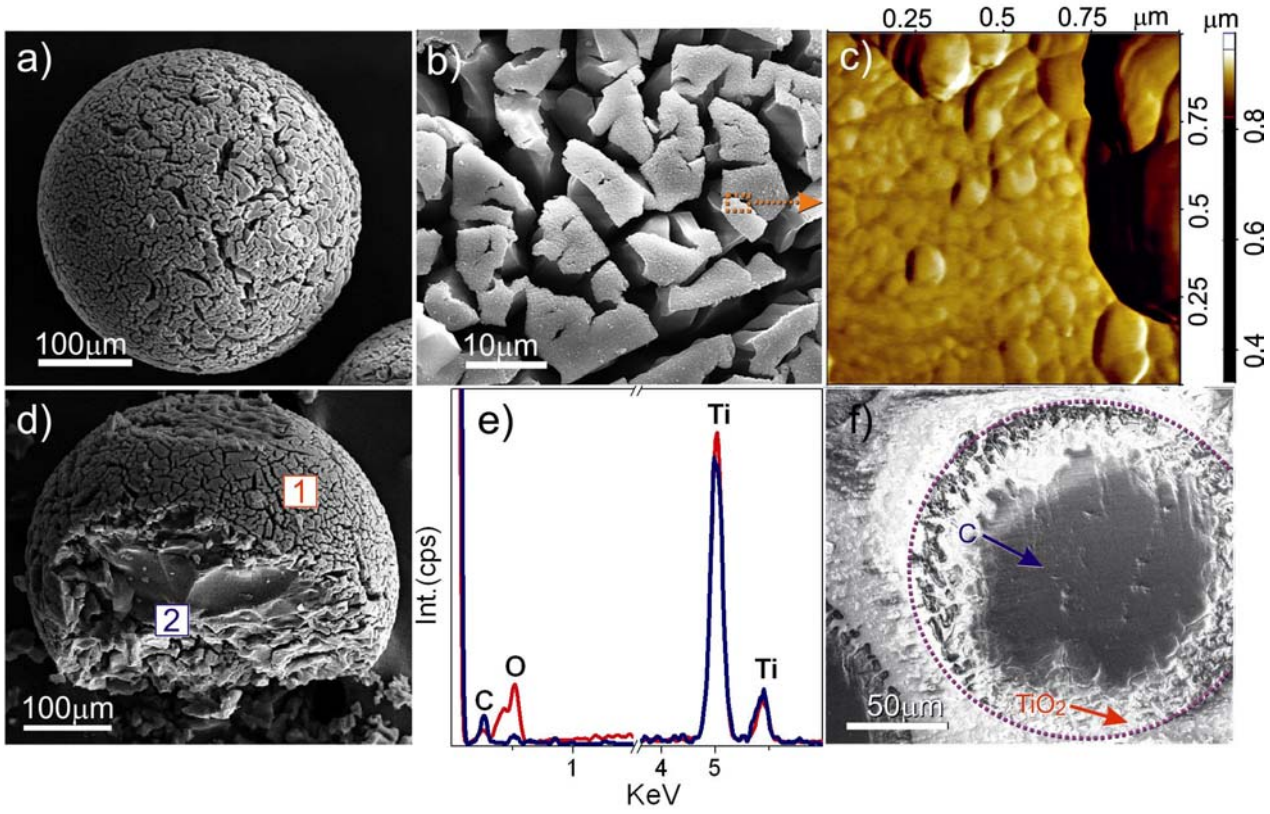

Figure 3. a) and b) SEM and c) AFM images of polymer microspheres after mild oxidation under N_2/air at 500°C for 15 min, taken at increasing magnification; d) SEM image of a fractured microsphere that exposes both the external and the inner part; e) chemical composition taken on the two selected regions of d): 1 (external, red) and 2 (internal, blue); f) cross section of the core shell C/TiO_2 microsphere after being embedded in an epoxy resin and cut. The peculiar contrast of f) refers to the different charging properties associated with C and with TiO_2 phases.

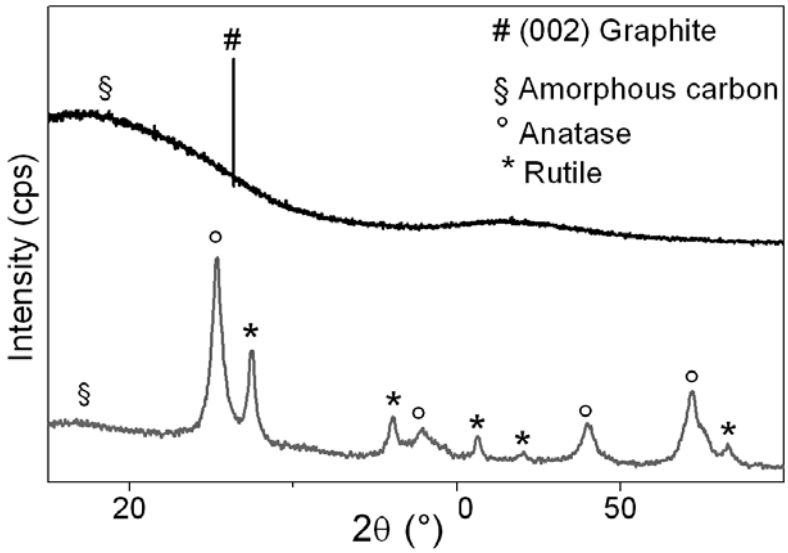

Figure 4. a) and b) XRD pattern of microspheres obtained upon thermal treatment at 500°C under N_2 and N_2/air gas mixture, respectively. XRD peak positions of reference standards are also reported (Graphite: #, Anatase: °, Rutile: *:).

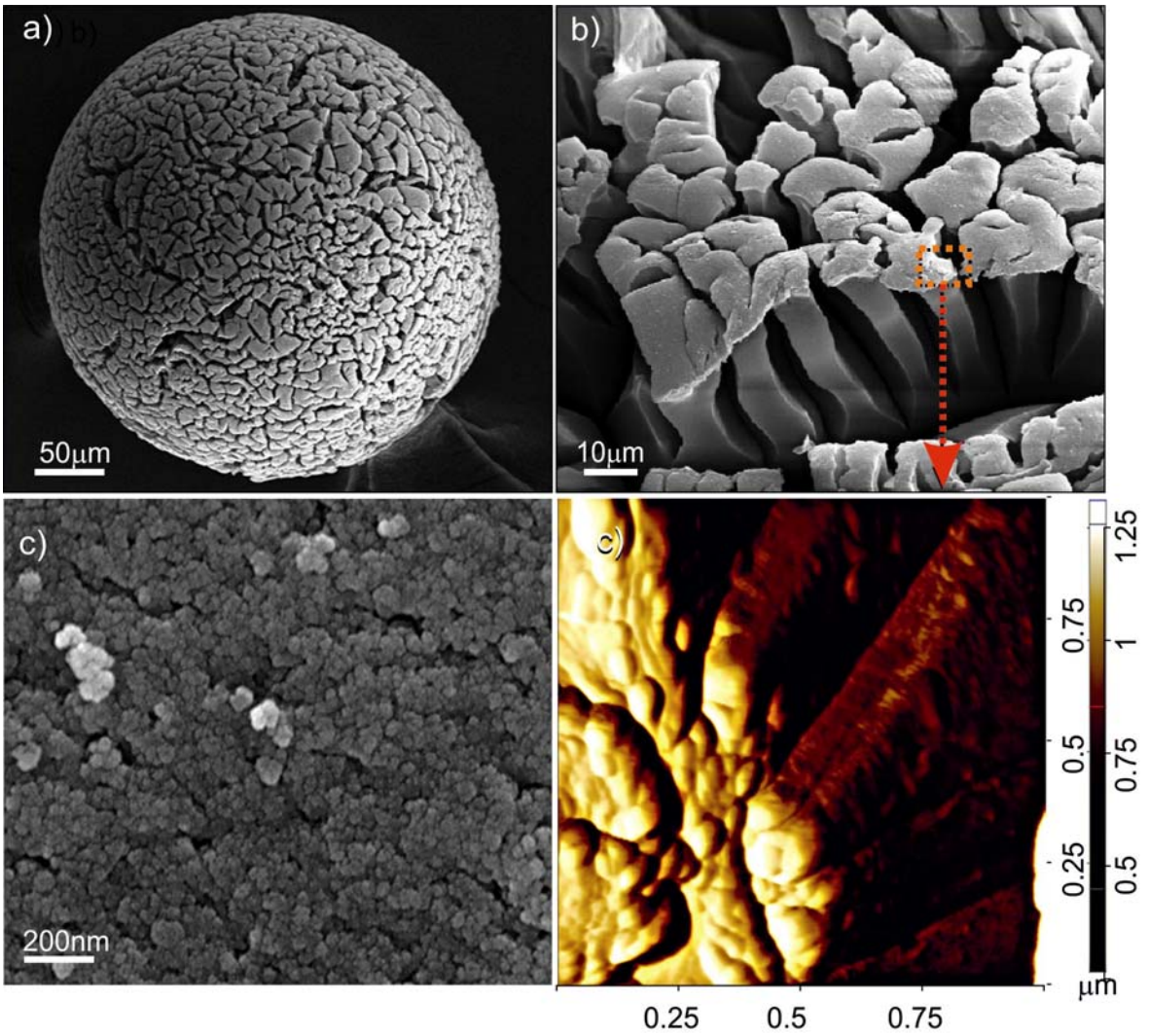

Figure 5. a) and b) SEM images of polymer microspheres after mild oxidation under N_2/air at 500°C for 2h, taken at increasing magnification; c) SEM top view and d) AFM images of an edge of a pillar, respectively.

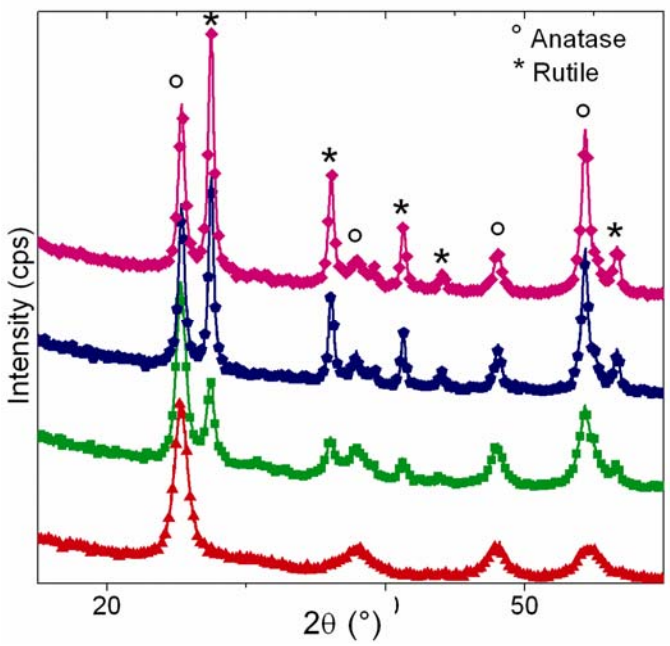

Figure 6. XRD patterns of microspheres obtained under complete oxidation at 400°C (red, triangles), 450°C (green, squares), 475°C (blue, pentagons) and at 500°C (magenta, rombs). XRD peaks marked by circles and asterisks are assigned to Anatase and Rutile, respectively.

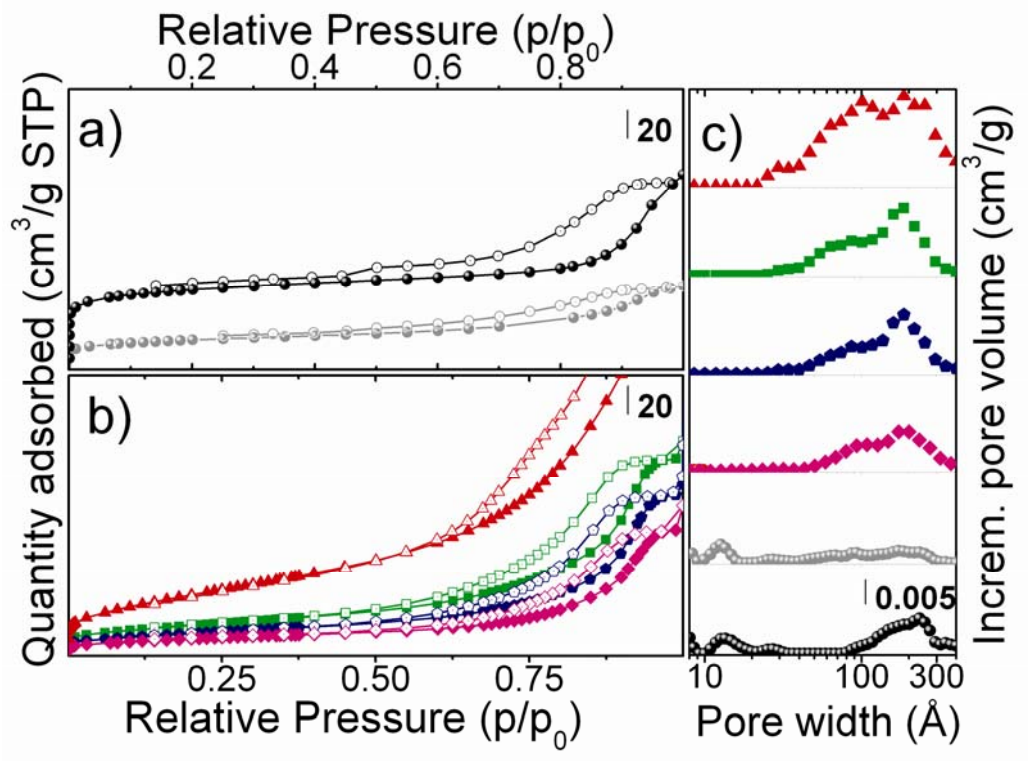

Figure 7. a) Volumetric N_2 adsorption/desorption isotherms at 77 K of samples obtained by thermal treatments in N_2 for 2h (black circles) and in air at 500°C for 15 min (gray circles) for 2h at 500°C. b) the same for samples oxidized at 400°C, 450°C 475°C and 500°C (magenta, blue, green and red

circles), respectively. Filled and empty scatters refer to the adsorption and desorption brunches, respectively. c) Pore distributions (PSDs) were obtained by applying the DFT method.

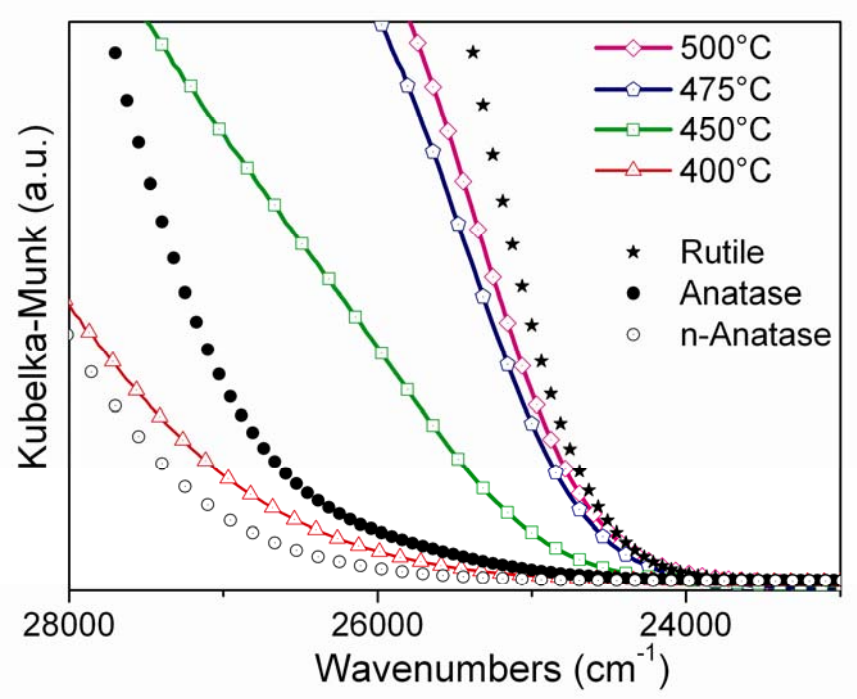

Figure 8. Diffuse-reflectance spectra of the TiO_2 microspheres obtained at different oxidation temperatures, as compared to reference materials: nanoanatase (crystal size in the 5-25 nm range, black empty cycles), anatase and rutile (crystal sizes in the 200-300 nm and 500-1000 nm ranges, black dots and black stars, respectively).

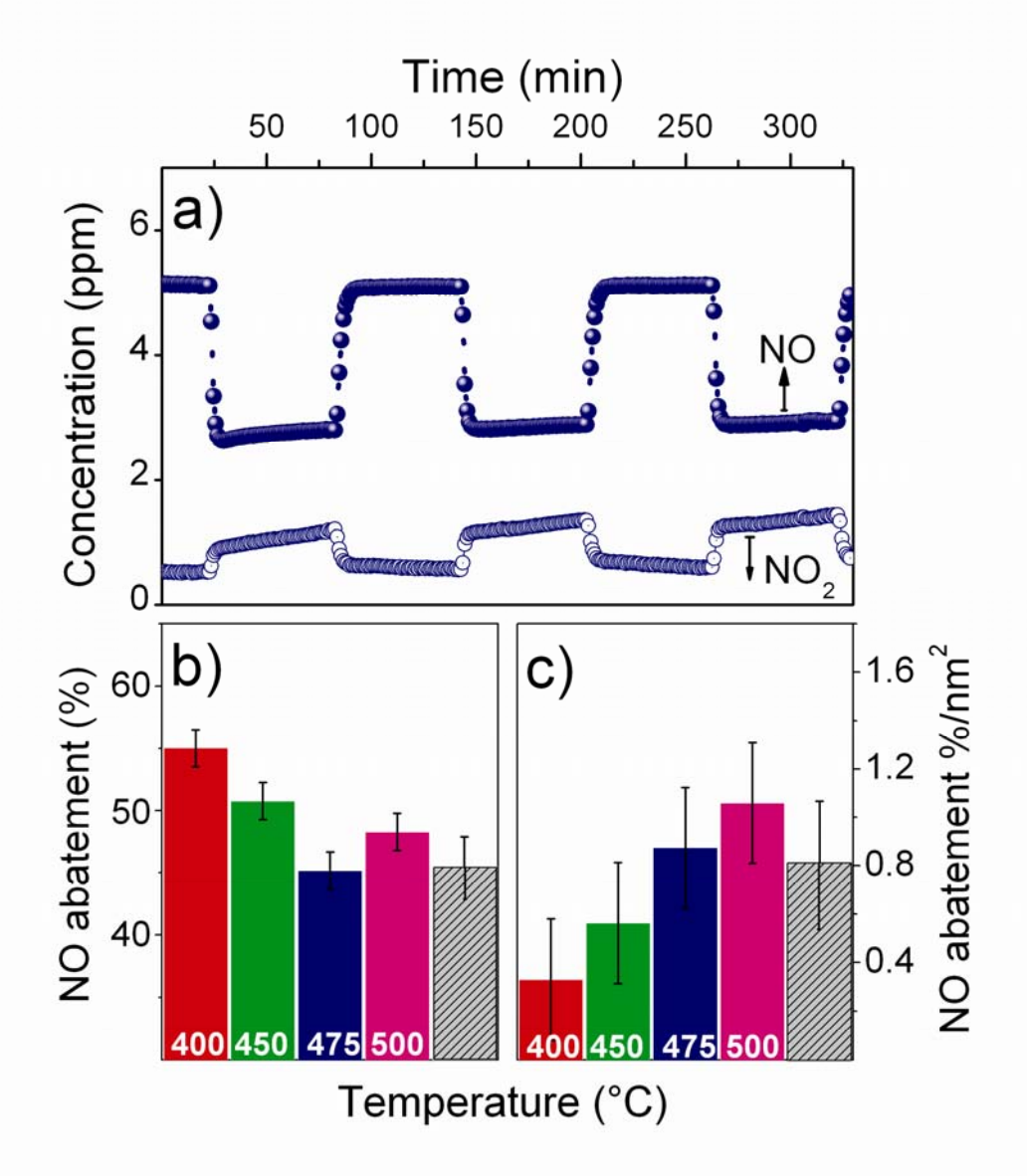

Figure 9. NO-photodegradation test for a TiO_2 sample obtained under alternated light irradiation/dark exposure: a) concentration evolution of NO and NO_2 as function of time; b) percentages of NO abatement for TiO_2 microspheres synthesized at different temperatures: 400°C (red), 450°C (blue), 475°C (green) and 500°C (magenta), as compared to P25 (gray); c) surface-area normalized activities of the data reported in b).

GRAPHICAL ABSTRACT